Article | Open Access

Energy Materials

Fu *et al. Energy Mater.* **2026**, *6*, 600127 **DOI:**10.20517/energymater.2026.211

Regulating Na^+ vacancies and stabilizing lattice structure via Al^{3+}/O^{2-} doping for low-cost dry-air-stable NaCl-based solid electrolytes

Chengyu Fu[1], Chenjie Lou[3], Liming Zhang[1], Longfei Li[1], Baozhang Li[4], Yi Sun[1], Mingxue Tang[3], Pengcheng Shi[2,*], Xuyong Feng[1,*], Hongfa Xiang[1,*]

Keywords:
Halide solid-state electrolytes, solid-state batteries, cubic crystal structure, low cost, dry air stability

Citation: Fu, C.; Lou, C.; Zhang, L.; Li, L.; Li, B.; Sun, Y.; Tang, M.; Shi, P.; Feng, X.; Xiang, H. Regulating Na^+ vacancies and stabilizing lattice structure via Al^{3+}/O^{2-} doping for low-cost dry-air-stable NaCl-based solid electrolytes. *Energy Mater.* **2026**, *6*, 600127. https://dx.doi.org/10.20517/energymater.2026.211

Received: 7 Jul 2026
First Decision: 27 Jul 2026
Revised: 3 Sep 2026
Accepted: 7 Sep 2026
Published: 24 Sep 2026

Academic Editor: Yuping Wu
Copy Editor: Fangling Lan
Production Editor: Fangling Lan

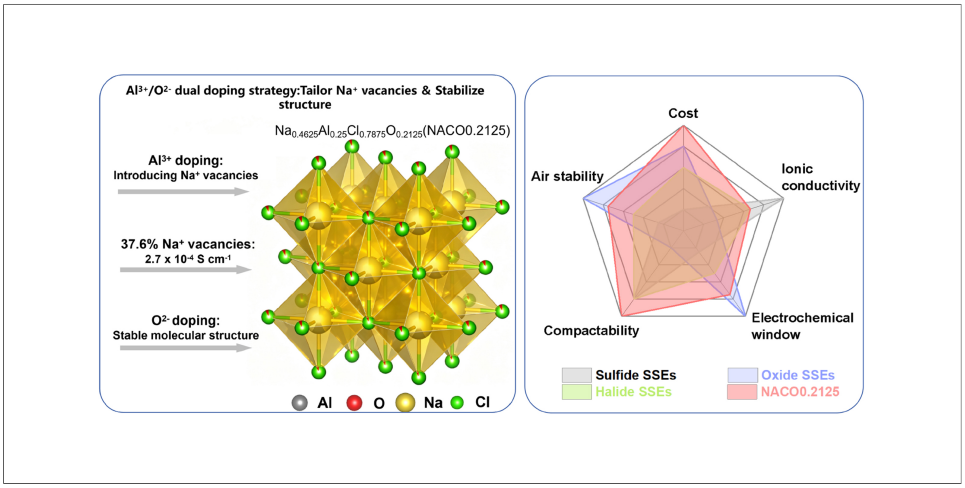

Abstract

Sodium chloride (NaCl) is attractive as a solid electrolyte because of its wide electrochemical stability window, excellent dry-air stability, favorable cathode compatibility, and low cost; however, its intrinsically low ionic conductivity has severely limited practical application. Here, we report an Al^{3+}/O^{2-} co-doping strategy that introduces Na^+ vacancies and mixed Cl^-/O^{2-} anion environments into the NaCl lattice, thereby converting NaCl from a poor ionic conductor into a fast-ion-conducting solid electrolyte. The optimized composition, $Na_{0.4625}Al_{0.25}Cl_{0.7875}O_{0.2125}$, exhibits an ionic conductivity of 2.7×10^{-4} S cm^{-1} at 30 °C. Through combined X-ray diffraction, solid-state nuclear magnetic resonance, and pair distribution function analysis, $Na_{0.4625}Al_{0.25}Cl_{0.7875}O_{0.2125}$ is identified as a single-phase face-centered cubic structure (space group *Fm*-3*m*) that hosts a high concentration of Na^+ vacancies (37.6%) at the 4*a* sites, creating a continuous 3D transmission network for rapid Na^+ migration. Electrochemically, $Na_{0.4625}Al_{0.25}Cl_{0.7875}O_{0.2125}$

[1]School of Materials Science and Engineering, Engineering Research Center of High-Performance Copper Alloy Materials and Processing, Ministry of Education, Hefei University of Technology, Hefei 230009, Anhui, China.
[2]School of Energy Materials and Chemical Engineering, Hefei University, Hefei 230601, Anhui, China.
[3]Center for High Pressure Science and Technology Advanced Research, Beijing 100193, China.
[4]Huacai New Energy Technology Co., Ltd., Hefei 230088, Anhui, China.

***Correspondence to:** Prof. Hongfa Xiang, Prof. Xuyong Feng, School of Materials Science and Engineering, Engineering Research Center of High-Performance Copper Alloy Materials and Processing, Ministry of Education, Hefei University of Technology, Hefei 230009, Anhui, China. E-mail: 2021800026@hfut.edu.cn or hfxiang@hfut.edu.cn; 2021800026@hfut.edu.cn; Prof. Pengcheng Shi, School of Energy Materials and Chemical Engineering, Hefei University, Hefei 230601, Anhui, China. E-mail: shipc@hfuu.edu.cn

exhibits a wide stability window of 1.05~4.24 V *vs.* Na_2Sn. In an all-solid-state cell with the configuration $NaNi_{1/3}Mn_{1/3}Ti_{1/3}O_2||Na_{0.4625}Al_{0.25}Cl_{0.7875}O_{0.2125}||Na_3PS_4||Na_2Sn$, capacity retentions of 89% and 83% are achieved after 100 cycles over voltage windows of 2.4-4.2 and 2.4-4.4 V, respectively.

INTRODUCTION

Solid-state electrolytes (SSEs) are the key component to realize advanced all-solid-state batteries (ASSBs), as they not only offer intrinsic safety but also effectively eliminate flammability hazards[1-6]. Sodium-based SSEs have attracted increasing interest because sodium is abundant and inexpensive, offering a potentially cost-effective platform for large-scale energy storage[7-9].

Drawing on the design principles established for liquid electrolytes, high-performance Na-based SSEs should combine high ionic conductivity, low activation barriers for ion migration, robust chemical and electrochemical stability, and favorable interfacial compatibility. From a commercialization perspective, low materials and processing costs are also essential[10-12]. Oxide-based SSEs (e.g., $Na_3Zr_2Si_2PO_{12}$ and Na-β-Al_2O_3)[13-16] can provide acceptable ionic conductivity and robust chemical stability, but they are limited by brittleness and high interfacial impedance[13,14]. Sulfide-based SSEs (e.g., Na_3PS_4, Na_3SbS_4, and $Na_{11}Sn_2PS_{12}$)[17-19] can achieve high ionic conductivity; however, they are hindered by a narrow electrochemical window and poor air stability[7]. Recently, crystalline halide-based SSEs are highly attractive due to superior ionic conductivity (10^{-4} to 10^{-3} S cm^{-1} at room temperature) and excellent cold-pressing deformability[20-23]. These advantages can balance the performance of sulfide- and oxide-based SSEs. However, previous studies on halide-based SSEs have primarily focused on low-symmetry crystal structures, such as trigonal and orthorhombic systems[24-27]. These halide-based SSEs usually suffer from insufficient air stability and high cost[28-33]. Meanwhile, these halide-based SSEs are still insufficient for applications due to limited cathode compatibility with oxidation potential below 4.0 V[34-37]. In this regard, novel sodium chloride (NaCl) based halide-based SSEs are highly competitive because of their wide electrochemical stability window, excellent dry air stability, favorable cathode compatibility (above 4.1 V) and extremely low cost[38,39]. Their practical development is nevertheless constrained by the intrinsically low ionic conductivity of the NaCl lattice.

In this work, we developed NaCl-based SSEs ($Na_{0.25+x}Al_{0.25}Cl_{1-x}O_x$, denoted as $NACO_x$, $0 \le x \le 0.225$) through an Al^{3+}/O^{2-} dual-ion doping strategy. The optimized $Na_{0.4625}Al_{0.25}Cl_{0.7875}O_{0.2125}$ ($NACO_{0.2125}$) SSEs present a single-phase face-centered cubic structure (space group *Fm*-3*m*). Specifically, the doping of Al^{3+} in the lattice can introduce abundant Na^+ vacancies (37.6%) at the *4a* sites, which provide fast transport channels for Na^+ migration. Meanwhile, O^{2-}, with a smaller ionic radius, can balance the cation-anion radius ratio in $NACO_{0.2125}$, stabilize the crystal structure of NaCl, and further enhance its dry air stability. Attractively, $NACO_{0.2125}$ exhibits an ionic conductivity of 2.7×10^{-4} S cm^{-1} at 30 °C and an electrochemical window of 1.05~4.24 V *vs.* Na_2Sn. The all-solid-state battery of $NaNi_{1/3}Mn_{1/3}Ti_{1/3}O_2||NACO_{0.2125}||Na_3PS_4||Na_2Sn$ demonstrates excellent cycling stability. When cycled at 0.3 C, it achieves a capacity retention of 89% after 100 cycles within 2.4~4.2 V. Even under a higher electrochemical window of 2.4~4.4 V, it still maintains a respectable capacity retention of 83%. This work opens up a new direction for the development of novel close-packed halide SSEs.

EXPERIMENTAL

Material synthesis

NaCl, $AlCl_3$, and NaOH were purchased from Sinopharm and used without further purification. $Na_{0.25+x}Al_{0.25}Cl_{1-x}O_x$ and $Na_{1-3y}Al_yCl$ were prepared by the same synthesis method. NaCl and $AlCl_3$ or NaCl,$AlCl_3$ and NaOH were milled with a NaCl:$AlCl_3$ molar ratio of (1-3y):y or with a NaCl:$AlCl_3$:NaOH

molar ratio of 0.25:0.25:x for 30 min. The pre-blended powder mixtures were sintered at 200 °C in a muffle furnace (Kejing, KSL-1400X-A1, China) for 2 h under a high-purity argon (Ar) atmosphere. The sintered products were subsequently subjected to high-energy ball milling in a 100 mL zirconia (ZrO_2) jar under vacuum at 550 rpm for 10 h using a planetary ball mill (Nanda Instruments, QM-3SP2, China). All sample handling and processing operations were conducted in an Ar-filled glovebox (Mikrouna, Super 750, China), where the contents of H_2O and O_2 were strictly controlled below 0.1 ppm to avoid contamination.

The Na_3PS_4 solid electrolyte was fabricated via a conventional solid-state synthesis route. Specifically, sodium sulfide (Na_2S, Sigma-Aldrich) and phosphorus pentasulfide (P_2S_5, 99% purity, Sigma-Aldrich) were weighed according to the stoichiometric ratio and homogeneously mixed by ball milling at 500 rpm for 12 h. The fully mixed powders were vacuum-sealed in a quartz tube and thermally annealed at 280 °C for 3 h to obtain the target electrolyte material.

The Na_2Sn anode material was synthesized through mechanical ball milling of metallic sodium (Na) and tin (Sn) powders (Sinopharm). Initially, the stoichiometric Na and Sn metal mixture was pre-rolled for preliminary blending, then transferred into a stainless-steel milling jar and hermetically sealed under Ar protection. The sealed mixture was ball-milled at 300 rpm for 10 h to yield a uniform Na_2Sn product. An additional 10 h of ball milling was performed if the obtained product exhibited an inhomogeneous morphology and composition.

Characterization

X-ray diffraction (XRD) experiments were performed using a Philips X'Pert powder diffractometer (Rigaku, D/MAX2500VL/PC, Japan) at 45 kV and 40 mA with Cu-K_α radiation (λ = 1.5406 Å). The samples were placed in a zero-background holder and sealed with a Kapton film to avoid air exposure. The data were collected at room temperature with 2θ from 10° to 80°. Rietveld refinement was carried out from XRD data with strong intensity. The following parameters were refined stepwise: (1) scale factor, (2) background using linear interpolation function with 10 coefficients, (3) peak shape using the pseudo-Voigt function, (4) unit cell parameters and fractional atomic coordinates, (5) fractional occupancy and thermal displacement parameters (Uiso). High-resolution synchrotron XRD and total scattering measurements were performed at beamline ID31 of the European Synchrotron Radiation Facility. NIST SRM 660b (NIST, LaB6, America) was used for geometry calibration. Scanning electron microscopy (SEM) images were conducted on a high-resolution field-emission scanning electron microscope (Hitachi, Regulus 8230, Japan). X-ray photoelectron spectroscopy (XPS) measurements were conducted on a Thermo Scientific K-Alpha instrument (Thermo Scientific, ESCALAB Qxi, China).

The ionic conductivity of all solid electrolytes was measured at 30 °C using electrochemical impedance spectroscopy (EIS) in the frequency range from 7 MHz to 1 Hz with a potential perturbation of 50 mV (Bio-Logic, SP-200, France). The activation energy was calculated based on variable-temperature impedance from room temperature up to 70 °C in a microclimate chamber. The as-synthesized solid electrolyte powders were pressed into pellets with a diameter of 12 mm, under a pressure of 370 MPa and then sandwiched between two steel rods for all measurements. The Young's modulus test was carried out on an Atomic Force Microscope (Bruker, Dimension ICON, Germany).

Linear sweep voltammetry (LSV) was employed to evaluate the electrochemical stability of the prepared SSEs. The working cathode was fabricated by blending the SSE powder with 10 wt% vapor-grown carbon fibers (VGCF). The assembled battery configuration adopted $NACO_{0.2125}$ as catholyte, the as-prepared Na_3PS_4 as anolyte and Na_2Sn as the anode material. The $NACO_{0.2125}$-VGCF cathode (10 mg), $NACO_{0.2125}$ (70 mg), Na_3PS_4 (70 mg), and Na_2Sn anode (50 mg) were separately compacted at a pressure of 300 MPa to construct a

12 mm-diameter cylindrical cell. The LSV measurements were performed on a Biologic SP-200 electrochemical workstation at a constant scan rate of 0.1 mV/s, with a voltage testing window ranging from 0 to 5 V.

All-solid-state $NaNi_{1/3}Mn_{1/3}Ti_{1/3}O_2$||$Na_{0.4625}Al_{0.25}Cl_{0.7875}O_{0.2125}$||$Na_3PS_4$||$Na_2Sn$ battery was fabricated using the following procedure. The composite cathode was made by ball milling the mixture of $NaNi_{1/3}Mn_{1/3}Ti_{1/3}O_2$, $Na_{0.4625}Al_{0.25}Cl_{0.7875}O_{0.2125}$ and VGCF (50:50:5 in weight ratio) at 300 rpm for 30 min. The ASSB was made by co-pressing Na_2Sn anode (50 mg), Na_3PS_4 (70 mg) anolyte, $Na_{0.4625}Al_{0.25}Cl_{0.7875}O_{0.2125}$ (70 mg) catholyte and $NaNi_{1/3}Mn_{1/3}Ti_{1/3}O_2$ composite cathode (12 mg) together in order, and under 300 MPa. Battery tests were carried out on a Neware battery test system (Neware, CT-4008Q-100mA, China).

RESULTS AND DISCUSSION

Synthesis and characterization of $Na_{0.25+x}Al_{0.25}Cl_{1-x}O_x$

To generate Na^+ vacancies in the NaCl lattice, partial Na^+ substitution with high-valence cations was implemented. Considering the economic factor, Al^{3+} was chosen as the dopant, which is the most abundant metal element in nature ($Na_{1-3y}Al_yCl$, $0 < y \leq 0.2$). As shown in Supplementary Figure 1, XRD revealed that as the Al content increased, well-resolved diffraction peaks characteristic of the $NaAlCl_4$ phase appeared and gradually intensified[24]. This observation demonstrated that Al^{3+} ions could not fit into the NaCl structure. Instead, $AlCl_3$ reacted with the NaCl matrix and formed $NaAlCl_4$. This situation can be explained by Pauling's first rule, which states that the cation-to-anion radius ratio (r_c/r_a) is the primary determinant of the cation coordination geometry and polyhedron stability[40]. For NaCl-type structures belonging to the *Fm*-3*m* space group, Na^+ ions (102 pm) sit in the *4a* octahedral sites where a cation is coordinated by six Cl^- anions (181 pm) in a highly symmetrical packing scheme. The mismatch in ionic radius, especially between Al^{3+} (53.5 pm) and Na^+ (102 pm), hinders effective Na^+ vacancy creation, leading to low ionic conductivity, which is critical for understanding material limitations. This imbalance induces excessive lattice strain and disrupts the original coordination frameworks. The ionic conductivity of $Na_{1-3y}Al_yCl$ with impurities was hardly improved, as shown in Supplementary Figure 2.

It is important to note that Al^{3+} can achieve stable sixfold coordination in α-Al_2O_3 primarily due to the influence of O^{2-} size and electronegativity. The small ionic radius of O^{2-} (140 pm) and its high electronegativity work together to optimize the cation-to-anion radius ratio for Al^{3+}, making this coordination thermodynamically favorable[41]. The high electronegativity of O^{2-} exerts a strong polarizing effect, distorting the electron cloud of Al^{3+} and slightly increasing its effective ionic radius, which further stabilizes the sixfold coordination. Based on the theoretical insight, we proposed a dual-anion modification strategy that involves the simultaneous incorporation of Al^{3+} and O^{2-} into the NaCl lattice. The introduction of O^{2-} reduces the average ionic radius of the anionic sublattice, which tailors the cation-to-anion radius ratio to the critical range required for producing six-coordinate configurations and stabilizing the doping of Al^{3+} at the 4*a* site. The dual-anion approach overcame issues inherent with the traditional aliovalent doping method and led to a novel NaCl-type halide SSE, denoted as $Na_{0.25+x}Al_{0.25}Cl_{1-x}O_x$ ($NACO_x$) ($0 \leq x \leq 0.225$).

Upon the doping of O^{2-}, $NACO_x$ retains the FCC architecture with the *Fm*-3*m* space group, which is isostructural to the parent NaCl lattice [Figure 1A]. XRD characterization [Figure 1B] revealed that as the O^{2-} doping content increases, the intensity of diffraction peaks corresponding to the $NaAlCl_4$ impurity phase gradually decreases. This observation confirmed that O^{2-} doping promotes the incorporation of Al^{3+} into the NaCl lattice. When $x \geq 0.2125$, diffraction peaks associated with $NaAlCl_4$ were eliminated, verifying the formation of a single-phase FCC solid solution.

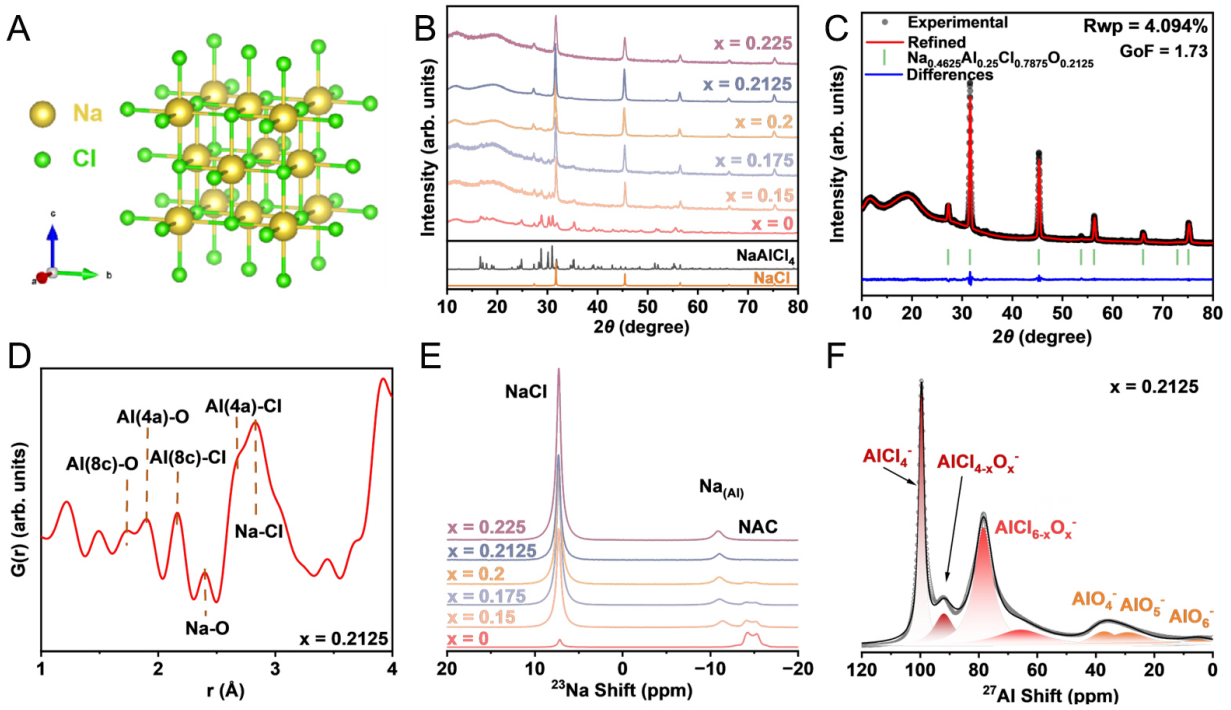

Figure 1. Structural characterization. (A) Crystal structure of NaCl; (B) XRD patterns of $Na_{0.25+x}Al_{0.25}Cl_{1-x}O_x$ ($0 \le x \le 0.225$); (C) Rietveld refinements of $Na_{0.4625}Al_{0.25}Cl_{0.7875}O_{0.2125}$; (D) PDF profiles of $Na_{0.4625}Al_{0.25}Cl_{0.7875}O_{0.2125}$; (E) ^{23}Na NMR of $Na_{0.25+x}Al_{0.25}Cl_{1-x}O_x$ ($0 \le x \le 0.225$). (F) ^{27}Al NMR of $Na_{0.4625}Al_{0.25}Cl_{0.7875}O_{0.2125}$.

XPS was first used to probe the local bonding environment of the phase-pure $Na_{0.4625}Al_{0.25}Cl_{0.7875}O_{0.2125}$ ($NACO_{0.2125}$) sample [Supplementary Figure 3]. Distinct Na-O and Al-O features were observed, indicating mixed Cl^-/O^{2-} coordination around Na and Al species[29,38]. When coupled with complementary XRD data [Figure 1B], these results provided compelling evidence that Al^{3+} and O^{2-} have been successfully doped into the NaCl lattice. To elucidate the atomic-scale structural features of the optimal single-phase composition, Rietveld refinement was performed on $NACO_{0.2125}$ [Figure 1C]. Based on the NaCl framework as a matrix, a partial substitution of Na^+ and Cl^- by Al^{3+} and O^{2-} occurred concurrently with the introduction of specific numbers of Na^+ vacancies. Subsequently, taking into account the large ionic radius difference between Al^{3+} and Cl^-, which drives the formation of $[AlCl_4]^-$, a part of Al^{3+} was incorporated at the tetrahedral *8c* sites to build the final structural model. The lattice constants, atomic coordinates, site occupancies, and isotropic displacement parameters were refined without additional constraints. The fitted curve aligned well with experimental data (Rwp = 4.094%), verifying both the rationality of the established structure and the sample purity, as no $NaAlCl_4$ impurity phases were observed. The refinement results confirmed a robust FCC framework with a high Na^+ vacancy concentration of 37.6% at the 4*a* sites, which constructs a continuous 3D percolation network for ion migration with a calculated Na^+ hopping distance of 3.98 Å. This unique structural configuration features a high density of interconnected Na^+ vacancies, which differs markedly from conventional halide SSEs and endows the $NACO_x$ system with enhanced ionic transport kinetics via the vacancy diffusion mechanism[42,43]. The refined lattice parameter is $a = b = c = 5.63$ Å, slightly smaller than that of pristine NaCl (5.64 Å), consistent with partial replacement of Na^+ (102 pm) by the smaller Al^{3+} cation (53.5 pm). A small fraction of Al also occupies the tetrahedral 8*c* sites, with a refined occupancy of 0.044 [Supplementary Table 1], indicating that Al^{3+} is distributed over both octahedral and tetrahedral environments.

To further resolve the local structure of $NACO_{0.2125}$, X-ray pair distribution function (PDF) analysis was performed [Figure 1D and Supplementary Figure 4]. The PDF spectrum of $NACO_{0.2125}$ in the high-*r* region

(r > 10 Å) closely matches that of pristine NaCl, indicating that the lattice structure remains intact, which supports confidence in the material's reliability despite Al^{3+}/O^{2-} co-doping[38]. In contrast, in the low-r region (r < 5 Å), the sensitivity to the short-range atomic coordination environment led to different characteristics and reflects the success of heteroatomic incorporation. Specifically, two prominent peaks centered at 2.83 and 2.40 Å were resolved in the PDF profile of $NACO_{0.2125}$, which are unambiguously assigned to the Na-Cl and Na-O bond pairs, respectively. The emergence of the Na-O signature peak provided direct structural evidence for the successful doping of O^{2-} anions into the halide lattice. Moreover, additional peaks at 2.16 and 1.73 Å correspond to Al-Cl and Al-O bonds in tetrahedral coordination environments, as confirmed by the Rietveld refinement results and corroborating the occupation of the tetrahedral 8*c* interstitial sites by a fraction of Al^{3+} ions. Further structural analysis identified peaks at 2.67 and 1.90 Å, which are attributed to Al-Cl and Al-O bond pairs associated with Al^{3+} ions residing in the octahedral 4*a* sites of the NaCl-type lattice. Notably, these bond lengths were slightly longer than the theoretical values for undoped analogs. This phenomenon can be rationalized by the strong polarization induced by the high charge density of Al^{3+} cations. This polarization distorts the electron cloud of adjacent anions, leading to a subtle expansion of the Al-anion coordination sphere[44,45]. Moreover, the atomic probability distribution derived from the PDF fitting clearly showed that the occupancy probability of Al^{3+} at the octahedral 4*a* sites is higher than that at the tetrahedral 8*c* sites. This result provides unambiguous quantitative evidence that over half of the doped Al^{3+} ions are successfully incorporated into the octahedral 4*a* sites of the NaCl lattice, thereby fully demonstrating the rationality of the defect-engineering design process.

Solid-state nuclear magnetic resonance (ssNMR) spectroscopy provided insights into the chemical coordination environments of Na^+ and Al^{3+} species[46], thereby delineating the structural evolution induced by the co-doping of Al^{3+} and O^{2-}. As illustrated in Figure 1E, the ^{23}Na NMR spectrum of the oxygen-free counterpart (x = 0) was dominated by a broad resonance spanning from -13 to -17 ppm, a characteristic chemical shift of Na^+ ions residing in the $NaAlCl_4$ phase. By contrast, only a faint signal at 7 ppm could be discerned, corresponding to Na^+ in the pristine NaCl lattice. This spectral feature confirmed the thermodynamic metastability of Al^{3+}-doped pristine NaCl, aligning with the XRD results [Figure 1B]. Upon the introduction of O^{2-} anions, the resonance intensity associated with the NaCl lattice was pronouncedly enhanced, demonstrating the positive impact of oxygen doping on lattice stability. Concomitantly, the signal attributable to the $NaAlCl_4$ phase gradually diminished until it was completely suppressed at the optimal doping stoichiometry of x = 0.2125. This spectral evolution provided unambiguous evidence for the formation of a single-phase NaCl-type solid solution, in excellent agreement with the phase identification results from XRD [Figure 1B]. Moreover, a distinct new resonance emerged at -11 ppm in the O^{2-}-doped samples, indicative of the formation of a novel Na^+ coordination environment within the SSE. This signal was attributed to the local environment of Na^+ adjacent to Al^{3+}. With the gradual increase in O^{2-} content, the higher electronegativity of O^{2-} relative to Cl^- exerted a stronger electrostatic effect, which induced a progressive downfield shift of the chemical shift[47,48].

The ^{27}Al NMR spectra further resolved the local coordination environments of Al^{3+} ions [Figure 1F]. Specifically, the sharp resonance centered at 100 ppm is characteristic of tetrahedrally coordinated Al^{3+} in the isolated $[AlCl_4]^-$ anion, while the peak at 92 ppm was assigned to the mixed-anion tetrahedral species $[AlCl_{4-x}O_x]^-$ formed via partial Cl^-/O^{2-} substitution. The peak at 78 ppm corresponded to octahedrally coordinated Al^{3+} in the mixed-anion polyhedron $[AlCl_{6-x}O_x]^-$, a configuration that was commensurate with the 4*a* crystallographic sites of the NaCl-type lattice. In addition, three minor peaks at 65, 36, and 4.6 ppm were unambiguously identified as the signatures of $[AlO_4]^-$, $[AlO_5]^-$, and $[AlO_6]^-$, respectively[49-52]. Quantitative deconvolution analysis of the ^{27}Al NMR spectra revealed that octahedral Al^{3+} species account for 65% of the total Al^{3+} species present in the system. This observation confirmed that the majority of Al^{3+} ions occupy the octahedral 4*a* sites of the NaCl-type framework, consistent with the design intent of our Al^{3+}/O^{2-} co-doping

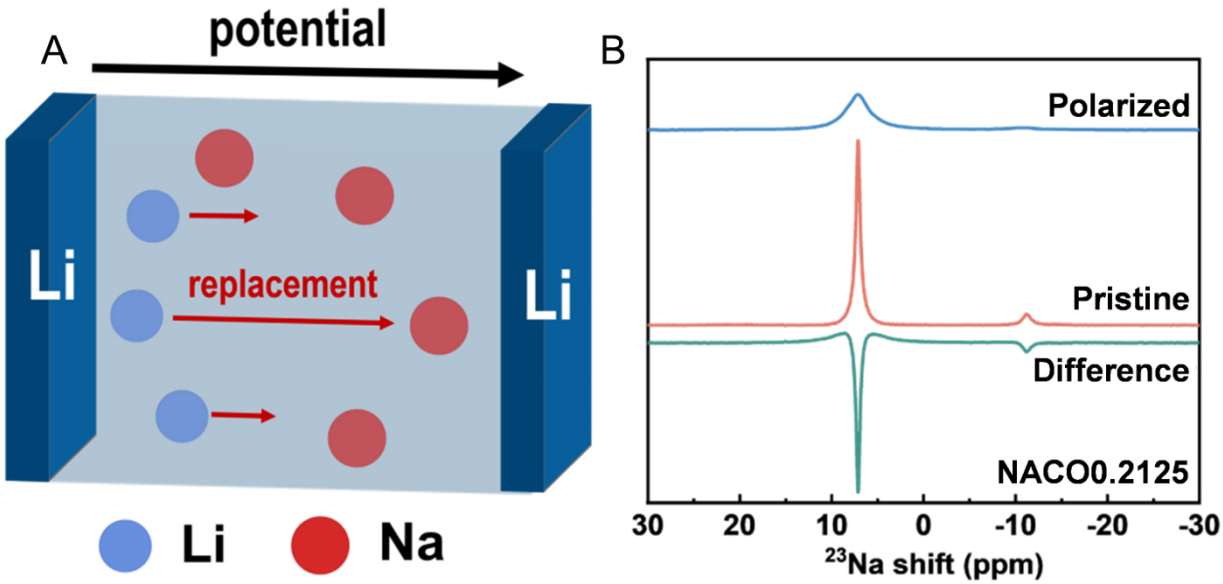

Figure 2. Transport mechanism analysis. (A) Li||$NACO_{0.2125}$||Li cell; (B) ^{23}Na MAS NMR of polarized and pristine $Na_{0.4625}Al_{0.25}Cl_{0.7875}O_{0.2125}$.

strategy. Meanwhile, the presence of tetrahedral Al-containing species (e.g., $[AlO_4]^-$, $[AlCl_{4-x}O_x]^-$) indicated that a minor fraction of Al^{3+} ions resides in the tetrahedral 8*c* interstitial sites of the FCC lattice. This preferential occupation of tetrahedral sites by a portion of Al^{3+} could be attributed to its small ionic radius (53.5 pm), which was better suited to the confined space of the 8*c* interstitial sites. Collectively, these ^{27}Al NMR results demonstrated that the $NACO_{0.2125}$ system does not adopt a simple, stoichiometric NaCl structure, but rather forms a complex substitutional solid solution with Al^{3+} ions distributed across both octahedral 4*a* and tetrahedral 8*c* sites. This refined atomic-scale structural model is in excellent agreement with the phase purity and lattice parameter analysis derived from Rietveld refinement and PDF results [Figure 1C and D], thereby providing a consistent structural basis for interpreting the ionic transport behavior of the $NACO_{0.2125}$ SSE.

To resolve the Na^+ transport mechanism within NaCl-type crystalline framework, we constructed Li||$NACO_{0.2125}$||Li symmetric cells and subjected them to a constant polarization bias [Figure 2A][53]. This experimental design capitalizes on the Li^+/Na^+ cation exchange reaction driven by Li^+ diffusion across the electrolyte. Specifically, the displacement of Na^+ from its original lattice sites under an external bias directly reveals the spatial distribution of active Na^+ migration channels. Incoming Li^+ can replace only Na^+ ions residing in transport-accessible sites. Notably, ^{23}Na NMR spectroscopy characterization of the polarized electrolyte [Figure 2B] revealed a pronounced decrease in the resonance intensities corresponding to the NaCl host lattice (7 ppm) and the $Na_{(Al)}$ local environment (-11 ppm), with the reduction ratio of the $Na_{(Al)}$ peak (59%) being markedly higher than that of the NaCl peak (18.1%). Such spectral evolution furnished unambiguous evidence for the construction of continuous Na^+ conduction channels within the electrolyte: Na^+ ions form a three-dimensional continuous ion transport network across the bulk lattice and exhibit a distinct tendency to migrate via the Na^+ vacancies adjacent to Al^{3+} sites. This result directly verified the efficacy of the defect engineering strategy proposed in this work.

Electrochemical performance and cost of $Na_{0.25+x}Al_{0.25}Cl_{1-x}O_x$

The optimized structural features of $NACO_{0.2125}$ (high Na^+ vacancy concentration and continuous 3D migration network) directly determine its electrochemical performance. Herein, we systematically evaluated the ionic conductivity, electrochemical stability window, and electronic conductivity of the $NACO_x$ series. Both ionic conductivity and phase purity showed a positive correlation with oxygen doping content over a

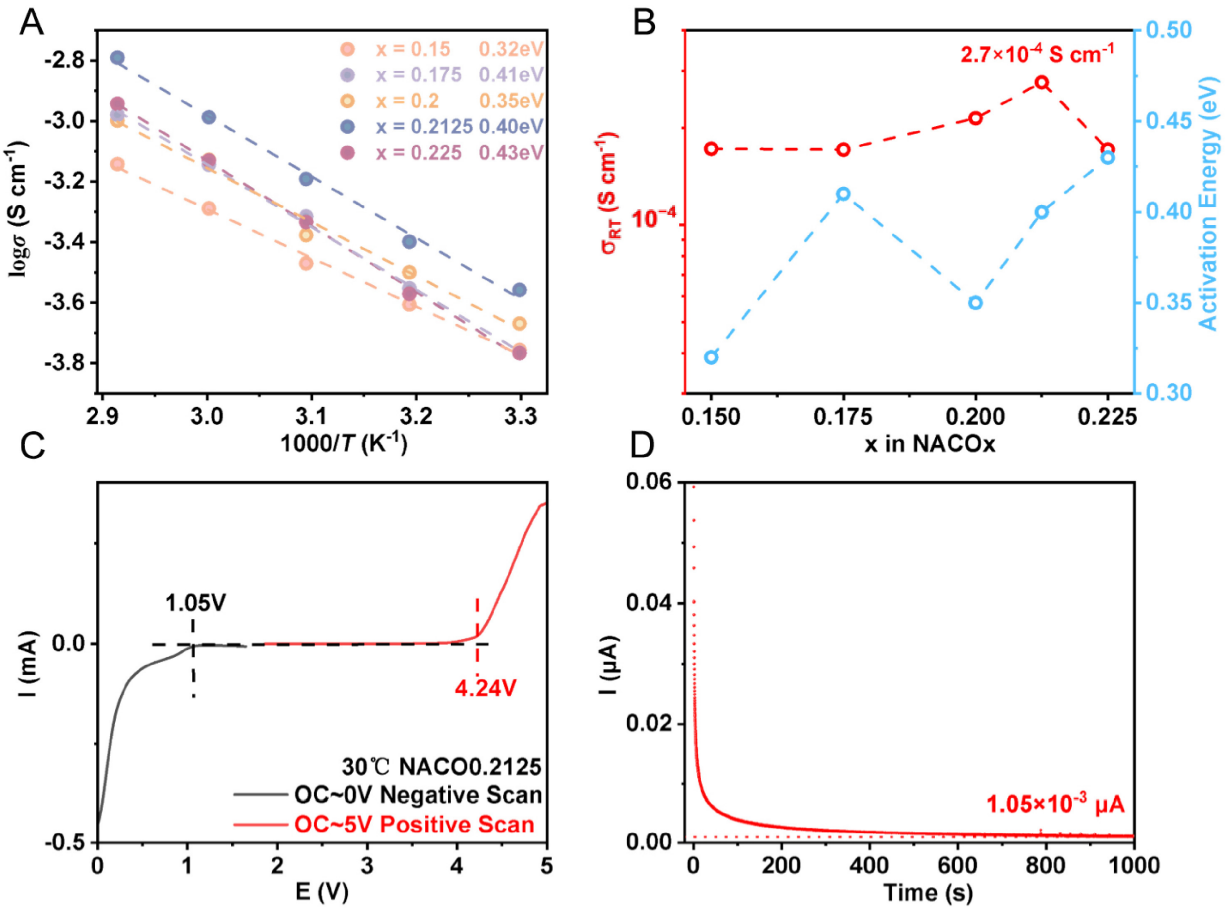

Figure 3. Electrochemical performance of $NACO_x$. (A) Arrhenius conductivity plots of $Na_{0.25+x}Al_{0.25}Cl_{1-x}O_x$ ($0.15 \leq x \leq 0.225$); (B) Ionic conductivities and activation energies of $Na_{0.25+x}Al_{0.25}Cl_{1-x}O_x$ ($0.15 \leq x \leq 0.225$); (C) Linear scanning voltammetry of $NACO_{0.2125}$ at 0.1 mV s^{-1}; (D) DC polarization curve of $NACO_{0.2125}$ under 0.2 V.

specific range. This trend arose primarily from the progressive suppression of the $NaAlCl_4$ impurity phase.

At the optimal doping stoichiometry of x = 0.2125, the composition achieved a maximum ionic conductivity of 2.7×10^{-4} S cm^{-1} at 30 °C [Figure 3A and B, Supplementary Figure 5]. This performance peak coincided with the high Na^+ vacancy concentration of 37.6% at the 4*a* sites, confirming that the vacancy-mediated diffusion mechanism affects ion transport in this system. In contrast, excessive oxygen doping (x = 0.225) triggered a decline in ionic conductivity to 1.7×10^{-4} S cm^{-1} at 30 °C [Supplementary Figure 5]. This deterioration could be ascribed to structural factors: the Na^+ vacancy concentration at the 4*a* sites decreased to 36.3%, thereby reducing the density of mobile charge carriers and raising the migration energy barrier[54,55]. On the other hand, increasing O^{2-} doping effectively reduces the content of $NaAlCl_4$ impurities, thereby improving the ionic conductivity of the $NACO_x$ samples [Supplementary Figure 5]. The optimal electrochemical performance is achieved at x = 0.2125, at which point impurity phases are completely eliminated. Further increasing the O^{2-} content causes a right shift of the XRD diffraction peaks for $NACO_{0.225}$ [Supplementary Figure 6]. Since O^{2-} possesses a smaller ionic radius than Cl^-, continuous oxygen substitution reduces the unit cell volume. This structural contraction distorts the Na^+ fast-migration pathways and ultimately deteriorates the ionic conductivity.

Electrochemical stability represents a pivotal metric for SSEs. To evaluate the electrochemical stability of $NACO_{0.2125}$, LSV measurements were performed on a tailored cell configuration: $NACO_{0.2125}$-VGCF||$NACO_{0.2125}$||Na_3PS_4||Na_2Sn, where Na_3PS_4 was introduced as an intermediate layer to mitigate direct

interfacial reactions between $NACO_{0.2125}$ and the Na_2Sn alloy anode. As illustrated in Figure 3C, the LSV profile reveals that $NACO_{0.2125}$ exhibits an electrochemical stability window spanning from 1.05-4.24 V (*vs.* Na_2Sn) at 30 °C. This wide oxidation stability up to 4.24 V surpasses that of most reported sodium-ion halide SSEs (typically 4.0-4.1 V), demonstrating its excellent stability with high-voltage cathode materials. Conversely, $NACO_{0.2125}$ shows limited reduction stability, with a noticeable increase in reductive current initiating at 1.05 V. This reductive decomposition behavior could be rationalized by the high electronegativity of Al^{3+} ions within the electrolyte lattice. To further confirm whether $NACO_{0.2125}$ inherits the reduction stability inherent to NaCl, symmetric $Na_2Sn||NACO_{0.2125}||Na_2Sn$ cells were assembled for subsequent performance testing [Supplementary Figure 7]. When cycled at a current density of 0.01 mA cm^{-2}, the cell exhibits significant voltage polarization, with the overpotential rising to 5 V or higher within 10 h of operation. This pronounced polarization stems from the continuous formation of resistive interfacial layers induced by the reductive decomposition of $NACO_{0.2125}$ at the anode-electrolyte interface. In addition to ionic conductivity, $NACO_{0.2125}$ exhibited an electronic conductivity as low as 3.8×10^{-10} S cm^{-1} [Figure 3D]. This ultra-low electronic conductivity effectively suppresses the risk of internal short circuits in ASSBs.

Another remarkable advantage of $NACO_{0.2125}$ lies in its extremely low cost. It can be synthesized via a simple preparation process using low-cost raw materials, namely NaCl, $AlCl_3$, and NaOH. Among these starting materials, $AlCl_3$ stands out for its exceptional economic viability, with a market price of merely 35.6 USD/kg [Supplementary Figure 8][56]. In addition, the market prices of NaOH and NaCl are as low as 6.41 and 0.10 USD/kg, respectively, resulting in an overall material cost for $NACO_{0.2125}$ of only 25.5 USD/kg[56]. When benchmarked against other Na-based SSEs reported in the literature, this value represents a remarkable cost superiority. Compared to the expensive Na_3PS_4 sulfide solid electrolytes and other halide solid electrolytes that use rare earth elements[56], $NACO_{0.2125}$ is extremely cheap, even cheaper than the already low-cost NASICON oxide electrolytes [Supplementary Figure 9].

Mechanical properties and dry air stability

Mechanical factors play a crucial role in the industrial fabrication and practical implementation of SSEs. These factors directly affect interfacial contact with electrodes, and long-term cycling durability in ASSBs. For $NACO_{0.2125}$, primary particle size analysis reveals a size distribution ranging from approximately 7 to 15 μm. Owing to the intrinsic cohesive nature of halide materials, these fine primary particles tended to aggregate spontaneously into secondary agglomerates with an average size of ~40 μm, as evidenced by morphological characterization [Supplementary Figure 10]. To quantitatively assess the mechanical performance of $NACO_{0.2125}$, atomic force microscopy (AFM) based nanoindentation measurements were conducted, with the representative modulus mapping and statistical analysis presented in Figure 4A and B, respectively. The morphological and mechanical data collectively demonstrate that $NACO_{0.2125}$ possesses an ultralow Young's modulus of ~ 2 GPa. This value is one order of magnitude lower than that of conventional inorganic SSEs (e.g., Na_3PS_4 with a Young's modulus of 20 GPa)[57,58] and is even comparable to the mechanical compliance of polymer-based SSEs (≤ 2 GPa)[59]. Such exceptional mechanical softness can be attributed to the formation of Al-O covalent bonds within the $NACO_{0.2125}$ lattice. Beyond Al-O mixed covalent-ionic bonds, multiple interrelated structural features synergistically reduce the Young's modulus of $NACO_{0.2125}$. First, the high density of Na^+ vacancies (37.6%) at octahedral 4*a* sites breaks the intact ionic bonding network of pristine NaCl, decreasing the total number of interatomic interactions per unit cell and weakening lattice stiffness. Second, mixed Cl^-/O^{2-} anion substitution introduces widespread local structural disorder and mild lattice distortion, disrupting long-range ordered ionic stacking and further lowering deformation resistance. Together with flexible Al-O bonds with low shear barriers, these three structural factors cooperatively endow $NACO_{0.2125}$ with an ultralow Young's modulus of ~2 GPa, enabling superior densification under compression. Under identical uniaxial pressing pressure, the cross-sectional morphology

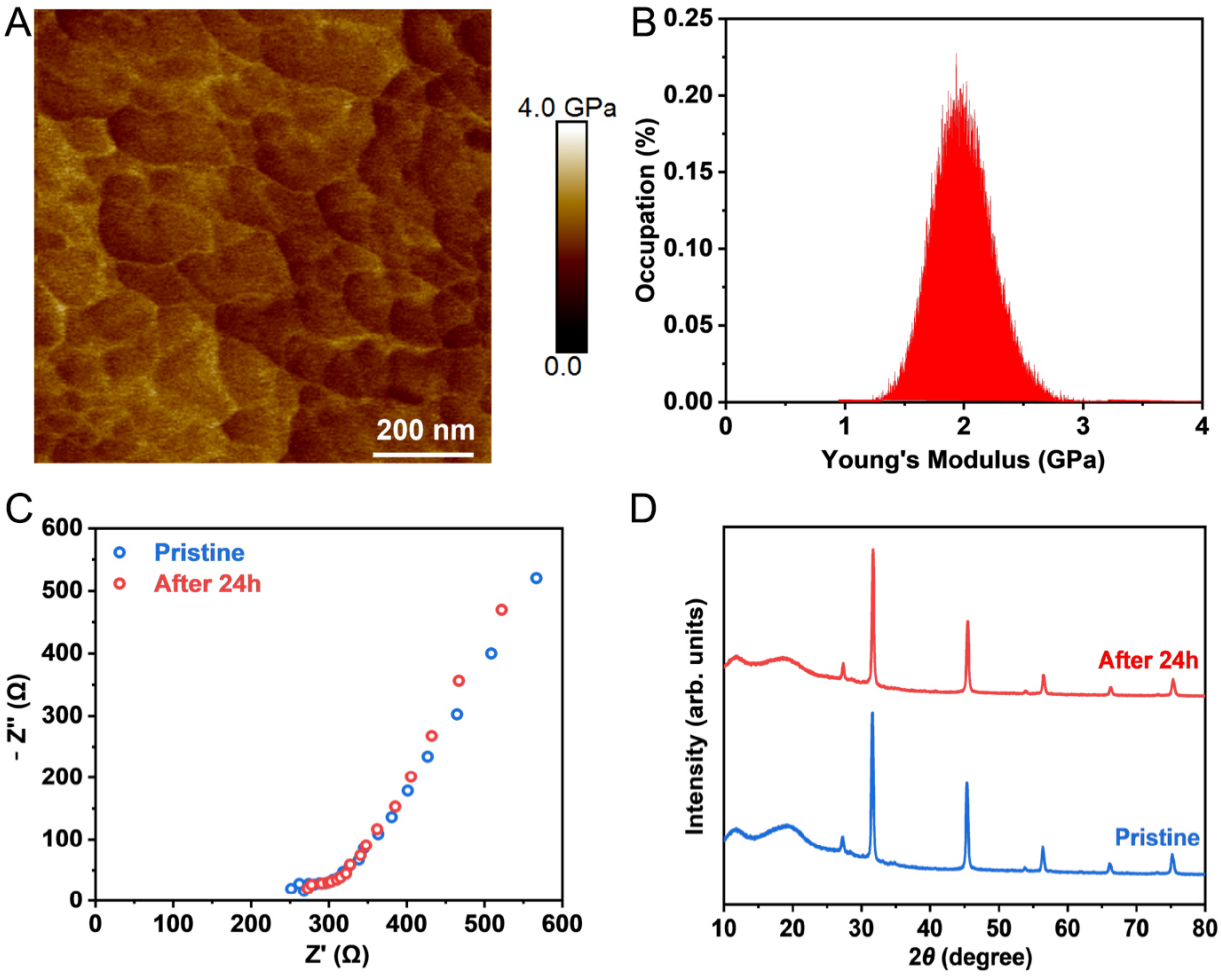

Figure 4. Chemical stability and mechanical properties. (A) AFM topography image of $NACO_{0.2125}$ pellet; (B) Young's modulus distribution of $NACO_{0.2125}$ pellet; (C) Nyquist plots of exposed $NACO_{0.2125}$; (D) XRD patterns of $NACO_{0.2125}$ and exposed $NACO_{0.2125}$ in dry air for 24 h.

of $NACO_{0.2125}$ pellets exhibited a highly dense and flat microstructure with negligible visible grain boundaries [Supplementary Figure 11A], whereas Na_3PS_4 pellets typically displayed distinct intergranular gaps and rough surfaces [Supplementary Figure 11B]. This enhanced densification capability facilitates intimate interfacial contact between the electrolyte and electrode materials, thereby minimizing interfacial resistance in assembled batteries. In addition, EIS measurements were performed on $NACO_{0.2125}$ pellets consolidated at various pressing pressures. As presented in Supplementary Figure 12, the $NACO_{0.2125}$ sample pressed at a low pressure of 200 MPa exhibits a moderate total resistance of 381 Ω, merely larger than that of the counterpart fabricated at 400 MPa (330 Ω). Benefiting from its low Young's modulus (~2 GPa), this electrolyte undergoes homogeneous plastic deformation upon compression and establishes intimate contact with electrode grains, effectively eliminating interfacial voids. These pressure-dependent EIS results solidly verify that the intrinsic mechanical compliance of NACO enables robust interfacial electrochemical properties even under low-pressure cell assembly conditions. Combined with its facile, cost-efficient synthesis protocol, the superior mechanical compliance of $NACO_{0.2125}$ renders it a far more industrially viable candidate than conventional halide SSEs.

Dry air stability is another important factor affecting the practical generation and application of SSEs. It is critical to clarify that the air stability characterization herein is performed under standardized industrial

dry-room conditions with a dew point of -40 °C, rather than uncontrolled humid ambient air at room temperature. Mass production of all-solid-state sodium batteries uniformly adopts -40~-60 °C dew dry rooms for electrolyte storage, powder transfer and pellet assembly, making this test condition practically relevant for industrial processing. After 24 h of exposure to an environment with a dew point of -40 °C, $NACO_{0.2125}$ powder exhibited a slight impedance rise from 280 to 300 Ω, corresponding to a mere 6.7% reduction in ionic conductivity [Figure 4C and Supplementary Figure 13]. Complementary XRD measurements further validated the structural robustness of $NACO_{0.2125}$ after dry air storage [Figure 4D]. In addition, XPS characterization results confirmed the absence of new characteristic peaks in the samples following exposure to the test environment [Supplementary Figure 14], providing further evidence of the excellent dry air stability of $NACO_{0.2125}$.

ASSBs using $NACO_{0.2125}$

Benefiting from the high ionic conductivity, wide stability window, and excellent mechanical compatibility, $NACO_{0.2125}$ is expected to serve as a practical SSE for ASSBs. Full cells with a high-voltage cathode $NaNi_{1/3}Mn_{1/3}Ti_{1/3}O_2$ and a Na_2Sn anode were assembled and evaluated. The composite cathode formulation consists of $NACO_{0.2125}$, $NaNi_{1/3}Mn_{1/3}Ti_{1/3}O_2$, and VGCF. After thorough mechanical mixing, the active material particles were uniformly dispersed together with $NACO_{0.2125}$ and VGCF in the composite cathode matrix [Supplementary Figures 11C and 15]. For the ASSB assembly, Na_3PS_4 (10^{-4} S cm^{-1}, Supplementary Figure 16) was introduced as an interlayer between the Na_2Sn anode [Supplementary Figure 11D] and the $NACO_{0.2125}$ electrolyte. The schematic diagram of the ASSB configuration is presented in Figure 5A. Cross-sectional morphological characterization of the assembled ASSB [Figure 5B and Supplementary Figure 17] reveals distinct layered structures with well-defined thicknesses: ~35 μm for the $NaNi_{1/3}Mn_{1/3}Ti_{1/3}O_2$ composite cathode, ~150 μm for the $NACO_{0.2125}$ electrolyte layer, ~175 μm for the Na_3PS_4 interlayer, and 45 μm for the Na_2Sn anode. Importantly, the composite cathode forms a tight interfacial bond with the $NACO_{0.2125}$ electrolyte layer, with no visible gaps at the interface. This superior interfacial contact is attributed to the excellent machinability of $NACO_{0.2125}$.

$NaNi_{1/3}Mn_{1/3}Ti_{1/3}O_2||NACO_{0.2125}||Na_3PS_4||Na_2Sn$ cell delivers stable cycling performance within a voltage window of 2.4~4.2 V, with an initial discharge capacity of 92.9 mAh·g^{-1} at 30 °C [Figure 5C]. Even after 100 cycles at 0.3 C, the battery retains a discharge capacity of 82.8 mAh g^{-1}, corresponding to a capacity retention rate of 89%. EIS measurements reveal that the initial impedance of the fresh full cell is 503 Ω, whereas the impedance surges to 1,100 Ω after 100 cycles [Supplementary Figure 18]. This impedance escalation induces electrochemical polarization, which is primarily responsible for the gradual capacity decay observed during long-term cycling. To elucidate the origin of this impedance growth, a compatibility study was conducted on the $NACO_{0.2125}/Na_3PS_4$ bilayer system: 100 mg pellets of $NACO_{0.2125}$ and Na_3PS_4 were fabricated separately under a pressure of 400 MPa and then stacked and aged for 72 h in an argon atmosphere. Post-aging impedance characterization shows an increase in the total interfacial impedance of the bilayer, providing direct evidence of chemical incompatibility between $NACO_{0.2125}$ and Na_3PS_4 [Supplementary Figure 19]. In addition, XRD analysis of the aged Na_3PS_4 showed the presence of impurity phases, confirming that side reactions occurred at the interface [Supplementary Figure 20]. This interfacial incompatibility is identified as one of the key factors contributing to the performance degradation of the full cell. Owing to the excellent oxidative stability of $NACO_{0.2125}$ (4.24 V *vs*. Na_2Sn), the ASSB based on this material enables stable cycling for 100 cycles at 0.3 C within the voltage window of 2.4~4.4 V, delivering an initial discharge capacity of 105.9 mAh g^{-1} and 83% capacity retention [Figure 5D and E]. In addition to cycling stability, the rate capability of the ASSB was evaluated to assess the dynamic ion transport behavior of $NACO_{0.2125}$ under different current conditions [Supplementary Figure 21]. At progressively increased current rates of 0.1, 0.2, 0.3, 0.5, and 1 C, the battery delivers discharge capacities of 116.2, 102.4, 88.0, 75.6, and 54.5 mAh g^{-1}, respectively. On the other hand, in this work, $NACO_{0.2125}$ was exposed to dry air for 24 h and then employed

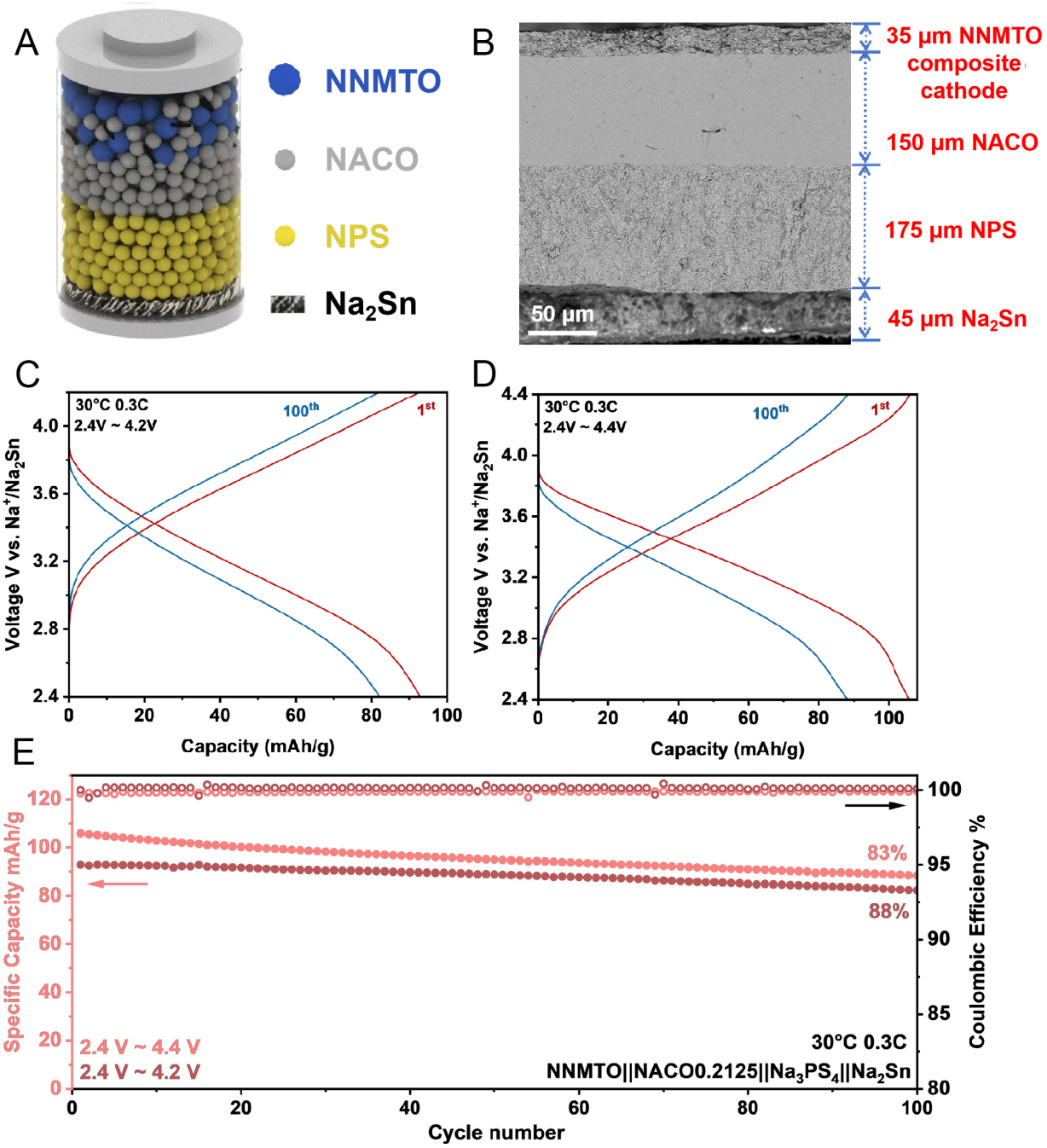

Figure 5. All-solid-state battery. (A) Configuration of ASSB with $NACO_{0.2125}$ as SSEs; (B) Cross-section SEM for different layers in the ASSB; (C) Charge-discharge profiles at different cycles (2.4~4.2 V); (D) Charge-discharge profiles at different cycles (2.4 V~4.4 V). (E) Cycle performance.

as an SSE in ASSBs to investigate the influence of air exposure. As presented in Supplementary Figure 22, the $NaNi_{1/3}Mn_{1/3}Ti_{1/3}O_2$||$NACO_{0.2125}$ (after exposure)||Na_3PS_4||Na_2Sn cell retained 86% of its initial capacity after 100 cycles at 0.3C. These results confirm that air-exposed $NACO_{0.2125}$ still exhibits satisfactory electrochemical performance in full cells, verifying its outstanding dry air stability. The battery performance showed the structural stability and high voltage compatibility of the $NACO_{0.2125}$-based ASSB system.

CONCLUSIONS

In summary, a novel NaCl-type halide solid electrolyte, $Na_{0.25+x}Al_{0.25}Cl_{1-x}O_x$, was designed and synthesized using an Al^{3+}/O^{2-} co-doping strategy. This approach effectively addresses the phase segregation issue commonly observed in traditional Al^{3+}-doped NaCl systems. Structural characterization techniques, including XRD, ssNMR, and PDF, confirmed that the optimal $NACO_{0.2125}$ composition forms a single-phase FCC structure, with Al^{3+} ions occupying both octahedral 4*a* and tetrahedral 8*c* sites. The incorporation of O^{2-} reduces the average anion radius, which facilitates the incorporation of Al^{3+} into the NaCl lattice. This optimization improves the distribution of sodium vacancies and enables the formation of a continuous three-dimensional ion transport network. Electrochemical characterization demonstrated that $NACO_{0.2125}$ exhibits high ionic conductivity (2.7×10^{-4} S cm^{-1} at 30 °C), ultra-low electronic conductivity, and a wide electrochemical stability window compatible with high-voltage cathode materials. Additionally, this material offers practical benefits, including a low Young's modulus (~ 2 GPa) for excellent compactibility, outstanding dry air stability, and a low raw-material cost (25.5 USD/kg). ASSBs based on $NACO_{0.2125}$ demonstrated stable cycling performance, with 89% capacity retention after 100 cycles in 2.4~4.2 V and 83% capacity retention in 2.4~4.4 V, validating the material's potential for practical battery applications. This study provides a promising paradigm for the rational design of low-cost, high-performance halide SSEs, thereby advancing the development of next-generation ASSBs.

DECLARATIONS

Acknowledgment

The analysis work of this article was partially carried out at the Instrumental Analysis Center, Hefei University of Technology.

Authors' contributions

Performed all experiments, analyzed the data, and wrote the original draft of the manuscript with input from all authors: Fu, C.; Shi, P.; Zhang, L.
Conducted XRD measurements and performed the rietveld refinements: Li, L.
Conducted the NMR measurements: Lou, C.
The manuscript was revised and edited: Fu, C.; Shi, P.; Feng, X.; Li, B.; Sun, Y.; Tang, M.
Conceived the study, provided the resources, and supervised the work: Feng, X.; Xiang, H.
All authors approved the final version of the manuscript.

Availability of data and materials

The data supporting the findings of this study are available within the article and its Supplementary Materials. The raw datasets generated and analyzed during the current study are available from the corresponding authors upon reasonable request.

AI and AI-assisted tools statement

Not applicable.

Financial support and sponsorship

This study was supported by the National Natural Science Foundation of China (U2330101 and 52302085), Taishan Industrial Leadership Talent Project (tscx202312052), the Major Science and Technology Projects in Anhui Province (2022e03020004 and 202423i08050026), the Key R&D Program of Anhui Province (2023t07020007), and the Fundamental Research Funds for the Central Universities (JZ2024HGTG0292), the innovation R&D Program of Anhui Province (202423i08050014), and the Major Science and Technology Projects in Anhui Province (2023z020003).

Conflicts of interest

Li, B. is affiliated with Huacai New Energy Technology Corp., while the other authors have declared that they have no conflicts of interest.

Ethical approval and consent to participate

Not applicable.

Consent for publication

Not applicable.

Copyright

Supplementary Materials

Supplementary Materials

REFERENCES

1. Pan, H.; Hu, Y.; Chen, L. Room-temperature stationary sodium-ion batteries for large-scale electric energy storage. *Energy. Environ. Sci.* **2013**, *6*, 2338. DOI
2. Bates, A. M.; Preger, Y.; Torres-Castro, L.; Harrison, K. L.; Harris, S. J.; Hewson, J. Are solid-state batteries safer than lithium-ion batteries? *Joule* **2022**, *6*, 742-55. DOI
3. Hirsh, H. S.; Li, Y.; Tan, D. H. S.; Zhang, M.; Zhao, E.; Meng, Y. S. Sodium-ion batteries paving the way for grid energy storage. *Adv. Energy. Mater.* **2020**, *10*, 2001274. DOI
4. Deysher, G.; Chen, Y.; Sayahpour, B.; et al. Evaluating electrolyte-anode interface stability in sodium all-solid-state batteries. *ACS. Appl. Mater. Interfaces.* **2022**, *14*, 47706-15. DOI PubMed PMC
5. Albertus, P.; Anandan, V.; Ban, C.; et al. Challenges for and pathways toward Li-metal-based all-solid-state batteries. *ACS. Energy. Lett.* **2021**, *6*, 1399-404. DOI
6. Li, C.; Li, R.; Liu, K.; Si, R.; Zhang, Z.; Hu, Y. S. NaSICON: a promising solid electrolyte for solid-state sodium batteries. *Interdiscip. Mater.* **2022**, *1*, 396-416. DOI
7. Kim, J. J.; Yoon, K.; Park, I.; Kang, K. Progress in the development of sodium-ion solid electrolytes. *Small. Methods.* **2017**, *1*, 1700219. DOI
8. Gao, H.; Xin, S.; Xue, L.; Goodenough, J. B. Stabilizing a high-energy-density rechargeable sodium battery with a solid electrolyte. *Chem* **2018**, *4*, 833-44. DOI
9. Razali A, Norazli SN, Sum WS, Yeo SY, Dolfi A, Srinivasan G. State-of-the-art of solid-state electrolytes on the road map of solid-state lithium metal batteries for E-mobility. *ACS. Sustain. Chem. Eng.* **2023**, *11*, 7927-64. DOI
10. Zhang, B.; Tan, R.; Yang, L.; et al. Mechanisms and properties of ion-transport in inorganic solid electrolytes. *Energy. Storage. Mater.* **2018**, *10*, 139-59. DOI
11. Banerjee, A.; Wang, X.; Fang, C.; Wu, E. A.; Meng, Y. S. Interfaces and interphases in all-solid-state batteries with inorganic solid electrolytes. *Chem. Rev.* **2020**, *120*, 6878-933. DOI
12. Su, H.; Jiang, Z.; Liu, Y.; et al. Recent progress of sulfide electrolytes for all-solid-state lithium batteries. *Energy. Mater.* **2022**, *2*, 200005. DOI
13. Rizvi, S.; Aladhyani, I.; Ding, Y.; Zhang, Q. Recent advances in doping N $Na_3Zr_2Si_2PO_{12}$ (NASICON) solid-state electrolyte for sodium-ion batteries. *Nano. Energy.* **2024**, *129*, 110009. DOI
14. Wang, J.; He, T.; Yang, X.; et al. Design principles for NASICON super-ionic conductors. *Nat. Commun.* **2023**, *14*, 5210. DOI PubMed PMC
15. Lu, X.; Xia, G.; Lemmon, J. P.; Yang, Z. Advanced materials for sodium-beta alumina batteries: status, challenges and perspectives. *J. Power. Sources.* **2010**, *195*, 2431-42. DOI
16. Wang, A.; Zhang, Q.; Li, W.; et al. Electrochemical-mechanical evolution of dendrites and cracks in $Na_3Zr_2Si_2PO_{12}$ ceramic solid electrolytes. *Adv. Energy. Mater.* **2025**, *15*, e02156. DOI
17. Hayashi, A.; Noi, K.; Sakuda, A.; Tatsumisago, M. Superionic glass-ceramic electrolytes for room-temperature rechargeable sodium batteries. *Nat. Commun.* **2012**, *3*, 856. DOI PubMed
18. Zhang, Z.; Ramos, E.; Lalère, F.; et al. $Na_{11}Sn_2PS_{12}$: a new solid state sodium superionic conductor. *Energy. Environ. Sci.* **2018**, *11*, 87-93. DOI
19. Zhang, L.; Zhang, D.; Yang, K.; et al. Vacancy-contained tetragonal Na_3SbS_4 superionic conductor. *Adv. Sci.* **2016**, *3*, 1600089. DOI PubMed PMC
20. Tan, Y.; Gatts, J.; Fu, C.; et al. Dual-anion sodium halide-based solid electrolytes with high ionic conductivity and high-voltage stability. *Small* **2025**, *21*, 2504677. DOI

21. Li, L.; Liu, S.; Li, S.; et al. Low-temperature heat recovery: an economic approach to renovate air-impaired $LiNbOCl_4$ electrolyte for boosted stability in high-performance all-solid-state batteries. *Chem. Eng. J.* **2025**, *526*, 171209. DOI
22. Zhou, L.; Bazak, J. D.; Li, C.; Nazar, L. F. 4 V Na solid state batteries enabled by a scalable sodium metal oxyhalide solid electrolyte. *ACS. Energy. Lett.* **2024**, *9*, 4093-101. DOI
23. Dai, T.; Wu, S.; Lu, Y.; et al. Inorganic glass electrolytes with polymer-like viscoelasticity. *Nat. Energy.* **2023**, *8*, 1221-8. DOI
24. Park, J.; Son, J. P.; Ko, W.; et al. $NaAlCl_4$: new halide solid electrolyte for 3 V stable cost-effective all-solid-state Na-ion batteries. *ACS. Energy. Lett.* **2022**, *7*, 3293-301. DOI
25. Kwak, H.; Lyoo, J.; Park, J.; et al. Na_2ZrCl_6 enabling highly stable 3 V all-solid-state Na-ion batteries. *Energy. Storage. Mater.* **2021**, *37*, 47-54. DOI
26. Schlem, R.; Banik, A.; Eckardt, M.; Zobel, M.; Zeier, W. G. $Na_{3-x}Er_{1-x}Zr_xCl_6$ - a halide-based fast sodium-ion conductor with vacancy-driven ionic transport. *ACS. Appl. Energy. Mater.* **2020**, *3*, 10164-73. DOI
27. Wu, E. A.; Banerjee, S.; Tang, H.; et al. A stable cathode-solid electrolyte composite for high-voltage, long-cycle-life solid-state sodium-ion batteries. *Nat. Commun.* **2021**, *12*, 1256. DOI PubMed PMC
28. Wang, L.; Song, Z.; Lou, X.; et al. $Na_{2.5}Cr_{0.5}Zr_{0.5}Cl_6$: a new halide-based fast sodium-ion conductor. *Small* **2024**, *20*, 2400195. DOI
29. Ridley, P.; Duong, G.; Ko, S. L.; et al. Tailoring chloride solid electrolytes for reversible redox. *J. Am. Chem. Soc.* **2025**, *147*, 19508-19. DOI PubMed PMC
30. Park, K.; Kaup, K.; Assoud, A.; Zhang, Q.; Wu, X.; Nazar, L. F. High-voltage superionic halide solid electrolytes for all-solid-state Li-ion batteries. *ACS. Energy. Lett.* **2020**, *5*, 533-9. DOI
31. Kwak, H.; Han, D.; Lyoo, J.; et al. New cost-effective halide solid electrolytes for all-solid-state batteries: mechanochemically prepared Fe^{3+}-substituted Li_2ZrCl_6. *Adv. Energy. Mater.* **2021**, *11*, 2003190. DOI
32. Li, X.; Liang, J.; Adair, K. R.; et al. Origin of superionic $Li_3Y_{1-x}In_xCl_6$ halide solid electrolytes with high humidity tolerance. *Nano. Lett.* **2020**, *20*, 4384-92. DOI
33. Gomes, B. M.; Baptista, M. C.; Orue, A.; et al. All-solid-state lithium batteries with NMC_{955} cathodes: PVDF-free formulation with SBR and capacity recovery insights. *Energy. Mater.* **2025**, *5*, 500091. DOI
34. Wang, J.; Chen, F.; Hu, L.; Ma, C. Alternate crystal structure achieving ionic conductivity above 1 mS cm^{-1} in cost-effective Zr-based chloride solid electrolytes. *Nano. Lett.* **2023**, *23*, 6081-7. DOI
35. Hu, L.; Wang, J.; Wang, K.; et al. A cost-effective, ionically conductive and compressible oxychloride solid-state electrolyte for stable all-solid-state lithium-based batteries. *Nat. Commun.* **2023**, *14*, 3807. DOI PubMed PMC
36. Duan, H.; Wang, C.; Zhang, X.; et al. Amorphous AlOCl compounds enabling nanocrystalline LiCl with abnormally high ionic conductivity. *J. Am. Chem. Soc.* **2024**, *146*, 29335-43. DOI
37. Li, Z.; Mu, Y.; Lü, K.; et al. Cation-anion-engineering modified oxychloride Zr-based lithium superionic conductors for all-solid-state lithium batteries. *Angew. Chem. Int. Ed.* **2025**, *64*, e202501749. DOI
38. Moeez, I.; Susanto, D.; Park, J. H.; Kim, J. Y.; Lim, H. D.; Chung, K. Y. Enhanced cycle stability of low-cost Na-rich metallic NaCl electrode for advanced Na-ion batteries. *Adv. Funct. Mater.* **2022**, *33*, 2210370. DOI
39. Yu, Q.; Hu, J.; Xu, Y.; Cao, R.; Chen, S.; Li, C. Mesoporous enhanced heterostructured halide solid electrolytes with high air stability and high abundance for sustainable sodium metal batteries. *Angew. Chem. Int. Ed.* **2025**, *64*, e202425503. DOI
40. Wei, Z.; Nazar, L. F.; Janek, J. Emerging halide solid electrolytes for sodium solid-state batteries: structure, conductivity, paradigm of applications. *Batteries. Supercaps.* **2024**, *7*, e202400005. DOI
41. Gibbs, G. V.; Ross, N. L.; Cox, D. F.; Rosso, K. M. Insights into the crystal chemistry of earth materials rendered by electron density distributions: pauling's rules revisited. *Am. Miner.* **2014**, *99*, 1071-84. DOI
42. Tian, H.; Dai, L.; Wang, L.; Liu, S. Interface stability control by an electron-blocking interlayer for dendrite-free and long-cycle solid sodium-ion batteries. *ACS. Sustain. Chem. Eng.* **2022**, *10*, 7500-7. DOI
43. Ma, C.; Yu, Z.; Fang, J.; et al. Coupled engineering of short-/long-range disorder in oxyhalides unlocks benchmark sodium superionic conductor. *Angew. Chem. Int. Ed.* **2025**, *65*, e18183. DOI
44. Yang, A.; Yao, K.; Schaller, M.; et al. Enhanced room-temperature Na^+ ionic conductivity in $Na_{4.92}Y_{0.92}Z_{r0.08}Si_4O_{12}$. *eScience* **2023**, *3*, 100175. DOI
45. Gao, K.; Bai, F.; Sun, Z.; Zhang, T. Aliovalent substitution of Al^{3+} in Li_2ZrCl_6 solid electrolyte towards large-scale application. *Energy. Storage. Mater.* **2024**, *70*, 103444. DOI
46. Rettenwander, D.; Blaha, P.; Laskowski, R.; et al. DFT study of the role of Al^{3+} in the fast ion-conductor $Li_{7-3x}Al_{3+x}La_3Zr_2O_{12}$ garnet. *Chem. Mater.* **2014**, *26*, 2617-23. DOI PubMed PMC

47. Ridley, P.; Nguyen, L. H. B.; Sebti, E.; et al. Amorphous and nanocrystalline halide solid electrolytes with enhanced sodium-ion conductivity. *Matter* **2024**, *7*, 485-99. DOI
48. Ruoff, E.; Kmiec, S.; Manthiram, A. Enhanced interfacial conduction in low-cost $NaAlCl_4$ composite solid electrolyte for solid-state sodium batteries. *Adv. Energy. Mater.* **2024**, *14*, 2402091. DOI
49. Düvel, A.; Romanova, E.; Sharifi, M.; et al. Mechanically induced phase transformation of γ-Al_2O_3 into α-Al_2O_3. Access to structurally disordered γ-Al_2O_3 with a controllable amount of pentacoordinated Al sites. *J. Phys. Chem. C.* **2011**, *115*, 22770-80. DOI
50. Wohlmuth, D.; Epp, V.; Bottke, P.; et al. Order*vs* disorder—a huge increase in ionic conductivity of nanocrystalline $LiAlO_2$ embedded in an amorphous-like matrix of lithium aluminate. *J. Mater. Chem. A.* **2014**, *2*, 20295-306. DOI
51. Zettl, R.; Gombotz, M.; Clarkson, D.; et al. Li-ion diffusion in nanoconfined $LiBH_4$-LiI/Al_2O_3: from 2D bulk transport to 3D long-range interfacial dynamics. *ACS. Appl. Mater. Interfaces.* **2020**, *12*, 38570-83. DOI PubMed PMC
52. Zhao, Z.; Xiao, D.; Chen, K.; et al. Nature of five-coordinated Al in γ-Al_2O_3 revealed by ultra-high-field solid-state NMR. *ACS. Cent. Sci.* **2022**, *8*, 795-803. DOI PubMed PMC
53. Feng, X.; Chien, P. H.; Zhu, Z.; et al. Studies of functional defects for fast na-ion conduction in $Na_{3-y}PS_{4-x}Cl_x$ with a combined experimental and computational approach. *Adv. Funct. Mater.* **2019**, *29*, 1807951. DOI
54. Pivarníková, I.; Seidlmayer, S.; Finsterbusch, M.; et al. Understanding the structure and mechanism of Na^+ diffusion in NASICON solid-state electrolytes and the effect of Sc- and Al/Y-substitution. *J. Mater. Chem. A.* **2025**, *13*, 14353-71. DOI
55. Kraft, M. A.; Gronych, L. M.; Famprikis, T.; Zeier, W. G. Influence of reduced na vacancy concentrations in the sodium superionic conductors $Na_{11+x}Sn_2P_{1-x}M_xS_{12}$ (M = Sn, Ge). *ACS. Appl. Energy. Mater.* **2021**, *4*, 7250-8. DOI
56. Zhang, L.; Lou, C.; Liang, S.; et al. Boosting ionic conductivity in $Li_xAlCl_{3-x}O_x$ solid electrolytes through anion-mixing-engineered ion diffusion channels. *Chin. Chem. Lett.* **2026**, *37*, 111558. DOI
57. Chi, X.; Zhang, Y.; Hao, F.; et al. An electrochemically stable homogeneous glassy electrolyte formed at room temperature for all-solid-state sodium batteries. *Nat. Commun.* **2022**, *13*, 2854. DOI PubMed PMC
58. Nose, M.; Kato, A.; Sakuda, A.; Hayashi, A.; Tatsumisago, M. Evaluation of mechanical properties of Na_2S-P_2S_5 sulfide glass electrolytes. *J. Mater. Chem. A.* **2015**, *3*, 22061-5. DOI
59. Shen, D.; Liang, W.; Wang, X.; et al. Lewis-basic nitrogen-rich covalent organic frameworks enable flexible and stretchable solid-state electrolytes with stable lithium-metal batteries. *Energy. Storage. Mater.* **2024**, *72*, 103709. DOI